Time-dependent covariant density functional theory in three-dimensional lattice space: Benchmark calculation for the $^{16}O + ^{16}O$ reaction

Z. X. Ren, P. W. Zhao,[*] and J. Meng[†]

State Key Laboratory of Nuclear Physics and Technology, School of Physics, Peking University, Beijing 100871, China

Time-dependent covariant density functional theory with the density functional PC-PK1 is developed in a three-dimensional coordinate space without any symmetry restrictions, and benchmark calculations for the $^{16}O + ^{16}O$ reaction are performed systematically. The relativistic kinematics, the conservation laws of the momentum, total energy, and particle number, as well as the time-reversal invariance are examined and confirmed to be satisfied numerically. Two primary applications including the dissipation dynamics and above-barrier fusion cross sections are illustrated. The obtained results are in good agreement with the ones given by the nonrelativistic time-dependent density functional theory and the data available. This demonstrates that the newly developed time-dependent covariant density functional theory could serve as an effective approach for the future studies of nuclear dynamical processes.

I. INTRODUCTION

During the past decades, new experimental facilities with radioactive beams have extended our knowledge of the nuclear chart to the very limits of nuclear binding, in particular to the unstable neutron-rich nuclei. Many novel and striking features have been found in the structure of neutron-rich nuclei, such as the halo phenomenon, and the disappearance of traditional magic numbers and occurrence of new ones [1,2]. The new observations not only provide us new insights for nuclear systems, but also challenge the established nuclear theory.

Enormous efforts have been made to understand the physics of nuclear many-body systems based on microscopic approaches. The nuclear density functional theory (DFT) is one of the most popular approaches in this context [3,4]. Starting from a universal energy density functional, the complicated nuclear many-body problem can be simplified as a one-body problem [5]. In this way, the DFT can provide a global description for almost all nuclei in the nuclear chart, including very neutron-rich nuclei, and a fairly good accuracy has been achieved with only a few parameters in the energy density functional.

By taking into account the Lorentz symmetry, the covariant density functional theory (CDFT) has attracted a lot of attention in nuclear physics [4,6–9]. In this framework, the nucleons are treated as Dirac particles moving in large scalar and vector fields of the order of a few hundred MeV [10]. This brings many advantages to describe nuclear systems with the CDFT, such as the new saturation mechanism of nuclear matter [11], the natural inclusion of spin-orbit interactions

[12], and, thus, the relativistic spin and pseudospin symmetries [13]. Another important advantage of the CDFT is the self-consistent treatment of the time-odd fields, which share the same coupling constants as the time-even ones thanks to the Lorentz invariance [7,14]. In the nonrelativistic DFT, while the Galilean invariance also constrains some time-odd fields, it does not work for those related to the square and the gradient of spin density [15]. With these advantages, CDFT has been successfully used to investigate the ground-state properties of many exotic nuclei [16–19] and also various nuclear excitation phenomena including rotations [20–23] and vibrations [24–27].

The time-dependent DFT (TDDFT) is a dynamical extension of DFT [28] for describing dynamical processes of many-body systems. In nuclear physics, the development of TDDFT can be traced back to the mid 1970s [29–36], which are known under the notation of the time-dependent Hartree-Fock method [37]. However, the early applications of the nuclear TDDFT suffered from simplified effective interactions and/or restricted geometric symmetries [38]. With ever-improving computational capabilities, the TDDFT experienced a revival during the last twenty years, and unrestricted three-dimensional (3D) calculations with modern nuclear density functionals became available [15,39–41]. To date, the TDDFT in 3D lattice space has been widely applied to many nuclear dynamical processes, such as the multinucleon transfer process [42–45], fission [46–49], fusion [50–54], collective vibration [55–57], cluster scattering [58], etc.

The dynamical extension of the CDFT, i.e., the time-dependent CDFT (TDCDFT), can be traced back to the early 1980s, where the time-dependent versions of the Walecka model were adopted to describe the dynamics of colliding nuclear slabs [59] and relativistic heavy ion collisions [60,61]. Later on, the time-dependent relativistic mean-field theory was used to describe the dynamics of Coulomb excitations

---
[*]pwzhao@pku.edu.cn
[†]mengj@pku.edu.cn

of nuclei by assuming axial symmetry [62,63]. In the present work, TDCDFT with the successful density functional PC-PK1 is developed in a three-dimensional coordinate space without any symmetry restrictions. This would be helpful to clarify the ambiguity of the spin-orbit fields and time-odd fields in the nonrelativistic TDDFTs and, thus, provide a new framework to investigate the dynamical processes of nuclei. However, such a development is not simple at all because of the longstanding difficulties in solving the CDFT in a 3D lattice [64,65]. Recently, the CDFT has been solved in a 3D lattice space with the inverse Hamiltonian [66,67] and Fourier spectral methods [68], and its successful applications include the studies of nuclear linear-chain [69] and toroidal structures [70]. This paves the way to develop the corresponding time-dependent approaches in a full 3D lattice space without assuming any symmetries.

In our very recent work [71], the TDCDFT was developed in a 3D lattice space with relativistic density functionals and applied to investigate the microscopic dynamics of the linear-chain cluster states. Following the previous work, a systematic investigation of the $^{16}\text{O} + ^{16}\text{O}$ reaction will be reported in this work with the detailed formalism of the TDCDFT in 3D lattice space. In Sec. II, the theoretical framework is introduced. The numerical details are given in Sec. III. Section IV is devoted to the numerical tests. Two primary applications, including the dissipation dynamics and above-barrier fusion cross sections, are presented in Secs. V and VI, respectively. Finally, a summary is given in Sec. VII.

II. THEORETICAL FRAMEWORK

A. Covariant density functional theory

The starting point of the CDFT is a standard Lagrangian density which, in the point-coupling form, can be written as [72]

$$
\begin{aligned}
\mathcal{L} &= \mathcal{L}^{\text{free}} + \mathcal{L}^{\text{4f}} + \mathcal{L}^{\text{hot}} + \mathcal{L}^{\text{der}} + \mathcal{L}^{\text{em}} \\
&= \bar{\psi}(i\gamma^\mu \partial_\mu - m_N)\psi - \frac{1}{2}\alpha_S(\bar{\psi}\psi)(\bar{\psi}\psi) \\
&\quad - \frac{1}{2}\alpha_V(\bar{\psi}\gamma^\mu\psi)(\bar{\psi}\gamma_\mu\psi) - \frac{1}{2}\alpha_{TV}(\bar{\psi}\vec{\tau}\gamma^\mu\psi)\cdot(\bar{\psi}\vec{\tau}\gamma_\mu\psi) \\
&\quad - \frac{1}{3}\beta_S(\bar{\psi}\psi)^3 - \frac{1}{4}\gamma_S(\bar{\psi}\psi)^4 - \frac{1}{4}\gamma_V[(\bar{\psi}\gamma^\mu\psi)(\bar{\psi}\gamma_\mu\psi)]^2 \\
&\quad - \frac{1}{2}\delta_S \partial^\nu(\bar{\psi}\psi)\partial_\nu(\bar{\psi}\psi) - \frac{1}{2}\delta_V \partial^\nu(\bar{\psi}\gamma^\mu\psi)\partial_\nu(\bar{\psi}\gamma_\mu\psi) \\
&\quad - \frac{1}{2}\delta_{TV}\partial^\nu(\bar{\psi}\vec{\tau}\gamma^\mu\psi)\cdot\partial_\nu(\bar{\psi}\vec{\tau}\gamma_\mu\psi) \\
&\quad - \frac{1}{4}F^{\mu\nu}F_{\mu\nu} - e\frac{1-\tau_3}{2}(\bar{\psi}\gamma^\mu\psi)A_\mu. \quad (1)
\end{aligned}
$$

It includes the Lagrangian density $\mathcal{L}^{\text{free}}$ for free nucleons, the four-fermion point-coupling terms $\mathcal{L}^{\text{4f}}$, the higher-order terms $\mathcal{L}^{\text{hot}}$ accounting for the medium effects, the derivative terms $\mathcal{L}^{\text{der}}$ to simulate the finite-range effects that are crucial for a quantitative description of nuclear density distributions, and the electromagnetic interaction terms $\mathcal{L}^{\text{em}}$. Thus, one can

build the energy density functional for a nuclear system,

$$
\begin{aligned}
E_{\text{tot}} &= E_{\text{kin}} + E_{\text{int}} + E_{\text{em}} \\
&= \int d^3 r \left\{ \sum_{k=1}^A \psi_k^\dagger(\boldsymbol{\alpha}\cdot\hat{\boldsymbol{p}} + \beta m_N)\psi_k + \frac{1}{2}\alpha_S\rho_S^2 + \frac{1}{3}\beta_S\rho_S^3 \right. \\
&\quad + \frac{1}{4}\gamma_S\rho_S^4 + \frac{1}{2}\delta_S\rho_S\Delta\rho_S + \frac{1}{2}\alpha_V j^\mu j_\mu + \frac{1}{4}\gamma_V(j^\mu j_\mu)^2 \\
&\quad + \frac{1}{2}\delta_V j^\mu \Delta j_\mu + \frac{1}{2}\alpha_{TV}j_{TV}^\mu(j_{TV})_\mu + \frac{1}{2}\delta_{TV}j_{TV}^\mu \Delta(j_{TV})_\mu \\
&\quad \left. + e j_c^\mu A_\mu + \frac{1}{2}A_\mu \Delta A^\mu \right\}, \quad (2)
\end{aligned}
$$

where E_{kin}, E_{int}, and E_{em} are the kinetic, interaction, and electromagnetic energies, respectively. The local densities and currents ρ_S, j^μ, j_{TV}^μ, and j_c^μ are given by

$$
\rho_s = \sum_{k=1}^A \bar{\psi}_k \psi_k, \quad (3a)
$$

$$
j^\mu = \sum_{k=1}^A \bar{\psi}_k \gamma^\mu \psi_k, \quad (3b)
$$

$$
j_{TV}^\mu = \sum_{k=1}^A \bar{\psi}_k \gamma_\mu \tau_3 \psi_k, \quad (3c)
$$

$$
j_c^\mu = \sum_{k=1}^A \bar{\psi}_i \gamma^\mu \frac{1-\tau_3}{2}\psi_k, \quad (3d)
$$

where τ_3 is the isospin Pauli matrix with the eigenvalues $+1$ for neutrons and -1 for protons. The time component j^0 is usually denoted as the vector density ρ_v.

In the static case, the densities and currents in Eq. (3) are time independent. By means of the variation of energy density functional Eq. (2) with respect to the densities and currents, one obtains the Kohn-Sham equation for nucleons,

$$
\hat{h}(\boldsymbol{r})\psi_k(\boldsymbol{r}) = \varepsilon_k \psi_k(\boldsymbol{r}), \quad (4)
$$

where ε_k is the single-particle energy and $\hat{h}$ is the single-particle Dirac Hamiltonian,

$$
\hat{h}(\boldsymbol{r}) = \boldsymbol{\alpha}\cdot(\hat{\boldsymbol{p}} - \boldsymbol{V}) + V^0 + \beta(m_N + S). \quad (5)
$$

The scalar $S(\boldsymbol{r})$ and four-vector $V^\mu(\boldsymbol{r})$ potentials read

$$
S(\boldsymbol{r}) = \alpha_S\rho_S + \beta_S\rho_S^2 + \gamma_S\rho_S^3 + \delta_S\Delta\rho_S, \quad (6a)
$$

$$
\begin{aligned}
V^\mu(\boldsymbol{r}) &= \alpha_V j^\mu + \gamma_V(j^\mu j_\mu)j^\mu + \delta_V \Delta j^\mu + \tau_3\alpha_{TV}j_{TV}^\mu \\
&\quad + \tau_3\delta_{TV}\Delta j_{TV}^\mu + e\frac{1-\tau_3}{2}A^\mu, \quad (6b)
\end{aligned}
$$

where the electromagnetic field A^μ is determined by Poisson's equation,

$$
-\Delta A^\mu = e j_c^\mu. \quad (7)
$$

By solving the Dirac equation Eq. (4) self-consistently, one can obtain the single-nucleon wave functions for a nucleus in its ground state.

B. Time-dependent covariant density functional theory

In the dynamical case, the evolution of single-nucleon wave functions ψ_k should fulfill the time-dependent Kohn-Sham equation [28,73],

$$i\frac{\partial}{\partial t}\psi_k(\boldsymbol{r}, t) = \hat{h}(\boldsymbol{r}, t)\psi_k(\boldsymbol{r}, t). \quad (8)$$

The time-dependent $\hat{h}(\boldsymbol{r}, t)$ is purely determined by the time-dependent densities and currents [28]. With the *adiabatic approximation* [40], the time-dependent single-particle Hamiltonian $\hat{h}(\boldsymbol{r}, t)$ in Eq. (8) is taken as the Dirac Hamiltonian in Eq. (5), in which the ground-state densities and currents, Eqs. (3), are obtained with the wave functions $\psi_k(\boldsymbol{r}, t)$ at the time t. This obviously lacks the memory effect, i.e., $\hat{h}(\boldsymbol{r}, t)$ does not depend on the history of the system.

The time-dependent Dirac Eq. (8) has the formal solution

$$\psi_k(\boldsymbol{r}, t) = \hat{\mathcal{T}} \exp\left[-i\int_{t_0}^{t} dt'\, \hat{h}(\boldsymbol{r}, t')\right]\psi_k(\boldsymbol{r}, t_0), \quad (9)$$

where $\hat{\mathcal{T}}$ represents the time-ordering operation and t_0 is the initial time.

For nuclear collisions, the initial wave functions $\psi_k(\boldsymbol{r}, t_0)$ are composed of the single-particle wave functions of the two nuclei, which are usually in their ground states, and are obtained from two separate static CDFT calculations. Subsequently, the two nuclei are placed on the mesh of a 3D lattice space with a large enough distance between them, so that the overlap between their wave functions is negligible at the initial time. Moreover, the nuclei are boosted to set them in motion.

As the Dirac equation is Lorentz covariant, the boost of nuclei can be realized by using the inhomogeneous Lorentz transformation [74]. Starting from the ground-state single-particle wave functions $\psi_k^{(\text{g.s.})}(\boldsymbol{r})$, the Lorentz boosted ones $\psi_k'(\boldsymbol{r})$ with velocity $\boldsymbol{v}$ read

$$\psi_k'(\boldsymbol{r}) = \hat{S}(\boldsymbol{v})\psi_k^{(\text{g.s.})}(\boldsymbol{r}')e^{i\varepsilon_k\boldsymbol{v}\cdot\boldsymbol{r}/\sqrt{1-v^2}}, \quad (10)$$

where $\hat{S}(\boldsymbol{v})$ denotes the transformation on the four components of a Dirac spinor,

$$\hat{S}(\boldsymbol{v}) = \sqrt{\frac{1+\sqrt{1-v^2}}{2\sqrt{1-v^2}}} + [\boldsymbol{\alpha}\cdot(\boldsymbol{v}/v)]\sqrt{\frac{1-\sqrt{1-v^2}}{2\sqrt{1-v^2}}}, \quad (11)$$

and $\boldsymbol{r}'$ represents the transformed coordinate,

$$\boldsymbol{r}' = \boldsymbol{r} + \left(\frac{1}{\sqrt{1-v^2}} - 1\right)\frac{(\boldsymbol{r}\cdot\boldsymbol{v})\boldsymbol{v}}{v^2}. \quad (12)$$

Note that here the single-particle energy ε_k is not shifted by the nucleon mass m_N.

The Lorentz boost in Eq. (10) can be connected with the Galilean boost used in the nonrelativistic TDDFT by approaching the nonrelativistic limits [$v/c \approx 0$ and $(\varepsilon_k - m_N)/m_N \approx 0$], under which the Lorentz boosted wave functions in Eq. (10) become

$$\psi_k'(\boldsymbol{r}) \approx \psi_k^{(\text{g.s.})}(\boldsymbol{r})e^{im_N\boldsymbol{v}\cdot\boldsymbol{r}}. \quad (13)$$

They are just identical with the Galilean boosted wave functions [75].

Finally, it should be mentioned that the spatial components of the electromagnetic vector potential $\boldsymbol{A}(\boldsymbol{r})$ are neglected in the calculations, since their contributions are extremely small. Although the center-of-mass correction energy is usually included *a posteriori* in the self-consistent static CDFT calculations, this strategy is disputable in the time-dependent case. For instance, it involves only the total mass number and does not account for the masses of the fragments. Therefore, similar to nonrelativistic TDDFT calculations, the center-of-mass correction is neglected in the present TDCDFT calculations.

III. NUMERICAL DETAILS

In the present work, the density functional PC-PK1 [72] is employed to study the $^{16}\text{O} + ^{16}\text{O}$ reaction. The Dirac spinors of the nucleons and the potentials are represented in 3D lattice space without any symmetry restriction. The mesh sizes along the x, y, and z axes are identical and chosen as $d = 0.8$ fm. The ground state of ^{16}O is calculated in a box with $24 \times 24 \times 24$ grid points, while for the time-dependent calculations a larger box with $30 \times 30 \times 50$ grid points is used. For the initial states of the time-dependent calculations, the centers of the two ^{16}O nuclei are placed in the z axis with a separation distance 16 fm. The Poisson equation for the Coulomb potential is solved by Hockney's method with the isolated boundary condition [76].

For the numerical implementation of the formal solution (9), the predictor-corrector strategy [75] is adopted, in which the evolution time is cut into a series of small time steps Δt. Over each time interval $[t, t + \Delta t]$, the single-particle Hamiltonian in Eq. (9) is approximated as the one at the mid-time $\hat{h}(t + \Delta t/2)$. Thus, the evolution of the single-particle wave function from t to $t + \Delta t$ is obtained as

$$\psi_k(\boldsymbol{r}, t + \Delta t) \approx \exp[-i\hat{h}(\boldsymbol{r}, t + \Delta t/2)\Delta t]\psi_k(\boldsymbol{r}, t), \quad (14)$$

which also provides the initial condition for the evolution over $[t + \Delta t, t + 2\Delta t]$.

In this work, the single-particle Hamiltonian $\hat{h}(t + \Delta t/2)$ is determined with a two-step recipe, i.e., first roughly constructed and then corrected to be a better one. In the first step, the densities and currents at time $t + \Delta t$, denoted generally as $\tilde{\rho}^{(1)}(t + \Delta t)$, are estimated from $\tilde{\psi}_k^{(1)}(\boldsymbol{r}, t + \Delta t)$,

$$\tilde{\psi}_k^{(1)}(\boldsymbol{r}, t + \Delta t) = \exp[-i\hat{h}(\boldsymbol{r}, t)\Delta t]\psi_k(\boldsymbol{r}, t). \quad (15)$$

The Hamiltonian $\hat{h}^{(1)}(\boldsymbol{r}, t + \Delta t/2)$ is roughly constructed using the average densities and currents $[\rho(\boldsymbol{r}, t) + \tilde{\rho}^{(1)}(\boldsymbol{r}, t + \Delta t)]/2$. In the second step, the obtained $\hat{h}^{(1)}(\boldsymbol{r}, t + \Delta t/2)$ is used to update the wave functions

$$\tilde{\psi}_k^{(2)}(\boldsymbol{r}, t + \Delta t) = \exp[-i\hat{h}^{(1)}(\boldsymbol{r}, t + \Delta t/2)\Delta t]\psi_k(\boldsymbol{r}, t), \quad (16)$$

which provide a new estimation for the densities and currents $\tilde{\rho}^{(2)}(t + \Delta t)$ at time $t + \Delta t$. The Hamiltonian $\hat{h}(\boldsymbol{r}, t + \Delta t/2)$ in Eq. (14) is then constructed from the average densities and currents $[\rho(\boldsymbol{r}, t) + \tilde{\rho}^{(2)}(\boldsymbol{r}, t + \Delta t)]/2$.

The exponential function of the Hamiltonian operator is evaluated by the Taylor expansion up to order m,

$$\exp(-i\hat{h}\Delta t)\psi \approx \sum_{n=0}^{m} \frac{(-i\Delta t)^n}{n!}\hat{h}^n\psi. \quad (17)$$
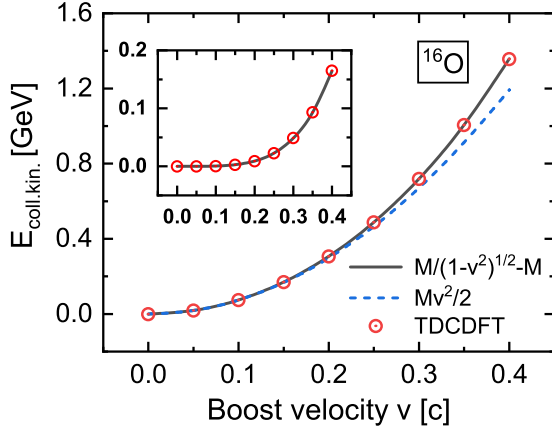
FIG. 1. The collective kinetic energy $E_{\text{coll. kin.}}$ of a boosted ^{16}O as a function of the boost velocity v. The open circles represent the collective kinetic energies obtained by TDCDFT. The solid and dashed lines denote the results of relativistic $M/(1 - v^2)^{1/2} - M$ and nonrelativistic kinetic $Mv^2/2$ energies (see text for the mass M), respectively. The inset shows the results after subtracting the nonrelativistic kinetic energies.

The values of $\Delta t = 0.1$ fm/c and $m = 4$ are adopted in the following calculations if not specified. A truncation of the Taylor expansion would violate the strict unitarity of $\exp(-i\hat{h}\Delta t)$ and energy conservation, so the conservation of particle number and energy should be checked carefully to preserve the quality of the time evolution.

IV. NUMERICAL TESTS

In this section, the TDCDFT benchmark calculations for the ^{16}O + ^{16}O reaction are performed in 3D lattice space. Numerical tests, including the collective kinetic energy as a function of boost velocity, the conservation of momentum, total energy, and particle number, as well as the time reversal invariance, are carefully examined.

The examinations are first focused on the tests involving a single ^{16}O. In Fig. 1, the collective kinetic energy $E_{\text{coll. kin.}}$ of a boosted ^{16}O is shown as a function of the boost velocity v, whose direction is set along the z axis. For comparison, the results of relativistic and nonrelativistic kinetic energies, i.e., $M/(1 - v^2)^{1/2} - M$ and $Mv^2/2$, are also shown, where the mass M of ^{16}O is evaluated from the ground-state total energy E_{tot} in Eq. (2). The TDCDFT results coincide with the relativistic kinetic energies very well, which is seen more clearly by subtracting the nonrelativistic kinetic energies (see the inset of Fig. 1). This shows that the adiabatic approximation for $\hat{h}(\boldsymbol{r}, t)$ in Eq. (8) is quite reasonable. The nonrelativistic kinetic energies deviate from relativistic ones dramatically with the velocity above $0.3c$. However, one should note that collisions at such high energies should not be described in time-dependent DFTs due to the mean-field approximation.

A boosted ^{16}O moves with a constant momentum. In TDCDFT, the momentum $\boldsymbol{p}(t)$ is represented by the expectation value of the momentum operator $\hat{\boldsymbol{p}}$. To examine the conservation of momentum, the ^{16}O is placed in the origin point and then is boosted with a collective kinetic energy
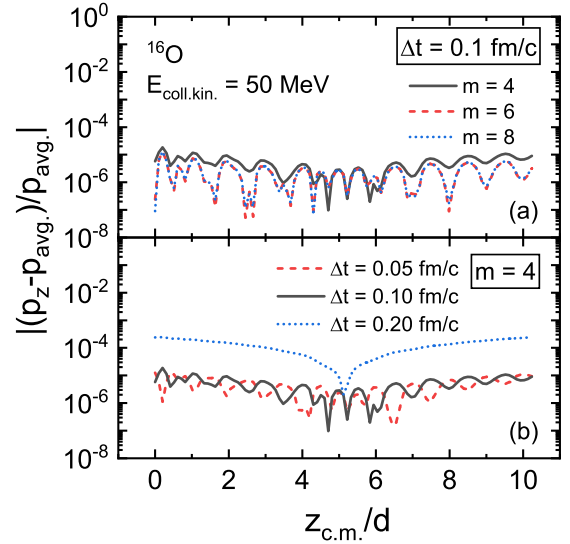

FIG. 2. The relative momentum deviation $|[p_z(t) - p_{\text{avg.}}]/p_{\text{avg.}}|$ with respect to the average momentum $p_{\text{avg.}}$ of a boosted ^{16}O as a function of the center-of-mass position $z_{\text{c.m.}}$. The abscissa is scaled by the mesh size d. The collective kinetic energy $E_{\text{coll. kin.}}$ for the boosted ^{16}O is set to 50 MeV. Panel (a) shows the results with the Taylor expansion orders $m = 4, 6, 8$ and the time evolution step $\Delta t = 0.10$ fm/c. Panel (b) shows the results with $\Delta t = 0.05, 0.10, 0.20$ fm/c and $m = 4$.

$E_{\text{coll. kin.}} = 50$ MeV along the z axis. The system is evolved for $T = 100$ fm/c. The average momentum along the z axis is estimated as

$$p_{\text{avg.}} = \frac{\int_0^T dt \, p_z(t)}{\int_0^T dt}. \tag{18}$$

Figure 2 shows the evolution of the relative momentum deviation $|[p_z(t) - p_{\text{avg.}}]/p_{\text{avg.}}|$ with Taylor expansion orders m and time evolution steps Δt as a function of the center-of-mass position $z_{\text{c.m.}}$, which is evaluated by

$$z_{\text{c.m.}} = \frac{\int d^3 r \, z \rho_v(\boldsymbol{r}, t)}{\int d^3 r \, \rho_v(\boldsymbol{r}, t)}. \tag{19}$$

The relative momentum deviation is reduced with larger m and smaller Δt. In the case of $\Delta t = 0.1$ fm/c and $m = 4$, the relative momentum deviations are as small as 10^{-5}, which reveals the accuracy of the momentum conservation. Even so, it is interesting to note that the relative momentum deviations oscillate with $z_{\text{c.m.}}$, because the space is not exactly translational invariant but is discretized on the lattices. In fact, the oscillation period is approximately the mesh size d.

Next, the conservation of total energy and particle number as well as the time reversal invariance for the ^{16}O + ^{16}O reaction are investigated. The head-on collision with a center-of-mass energy $E_{\text{c.m.}} = 50$ MeV is taken as an example.

In Fig. 3, the time evolutions of the relative energy deviation $|[E_{\text{tot}}(t) - E_{\text{init.}}]/E_{\text{init.}}|$ with different Δt and m values are shown. For $\Delta t = 0.1$ fm/c, the relative energy deviations are around 10^{-4} and 10^{-5} for $m = 4$ and 8, respectively.
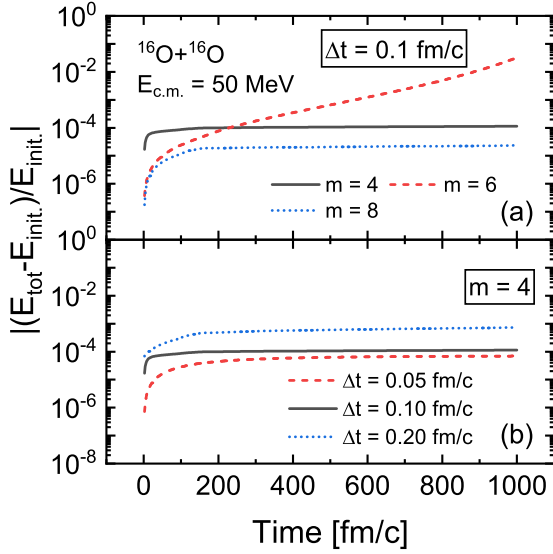
FIG. 3. The relative energy deviation $|[E_{tot}(t) - E_{init.}]/E_{init.}|$ with respect to the initial energy $E_{init.}$ for the $^{16}O + ^{16}O$ head-on collision at the center-of-mass energy $E_{c.m.} = 50$ MeV. The rest mass m_N for nucleons has been subtracted from the total energy E_{tot}. Panel (a) shows the results with the Taylor expansion orders $m = 4, 6, 8$ and the time evolution step $\Delta t = 0.10$ fm/c. Panel (b) shows the results with $\Delta t = 0.05, 0.10, 0.20$ fm/c and $m = 4$.

However, the evolutions of the relative energy deviation for $m = 6$ are not stable, in particular at longer time. The reason is not clear at the moment, but a similar phenomenon is also found in the calculation of nonrelativistic TDDFT [75]. It is very likely to be a numerical issue. In fact, the instability of evolution for $m = 6$ disappears at $\Delta t = 0.05$ fm/c. One may generally expect that the evolution becomes more stable for larger m values, while, for $\Delta t = 0.1$ fm/c, it is a little surprising that the evolution with a smaller $m = 4$ is quite stable. There seem to be subtle cancellations of numerical errors during the evolution. This is not a generic conclusion, and a careful test for the stability of time evolution should always be made before systemic calculations. For $m = 4$, the smaller the time evolution step Δt is, the better the total energy is conserved. This can be understood because the approximations in Eqs. (14) and (17) are better for smaller Δt values.

In Fig. 4, the evolution of the total energy is shown as a function of time, where $\Delta t = 0.1$ fm/c and $m = 4$ are adopted. The total energy is conserved along the time evolution at a precision of about 10^{-4}. The three energy constituents including the interaction energy E_{int}, the electromagnetic energy E_{em}, and the kinetic energy E_{kin} [see Eq. (2)], are also shown in Fig. 4. There are obvious fluctuations up to 70 MeV for these energy constituents, in particular for the interaction and kinetic energies, which could correspond to density oscillations of the excited composite system. Note that in the present covariant framework, the interaction energy E_{int} is determined by the densities and/or currents in the scalar and vector channels. The energy fluctuations in each channel are large and even beyond 1000 MeV. This reveals that the conservation of the total energy is indeed achieved by an elegant
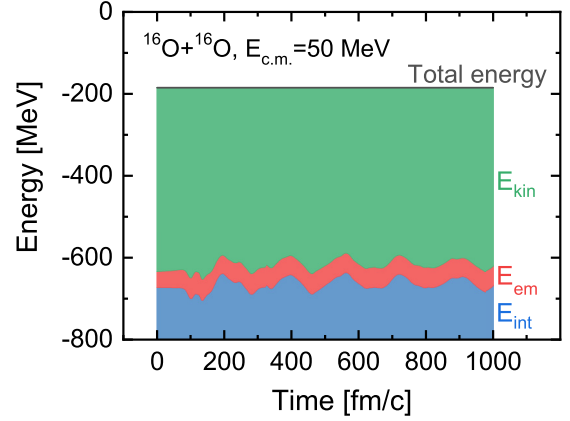

FIG. 4. Time evolution of the total energy and its constituents including the interaction energy E_{int}, the electromagnetic energy E_{em}, and the kinetic energy E_{kin}, for the $^{16}O + ^{16}O$ head-on collision at the center-of-mass energy $E_{c.m.} = 50$ MeV. The rest mass m_N for nucleons has been subtracted from the total and kinetic energies.

balance between two large energies in the scalar and vector channels.

Another important examination associated with the approximation in Eq. (17) is the conservation of the total particle number $N(t)$ with the definition:

$$N(t) = \int d^3r \, \rho_v(\mathbf{r}, t). \tag{20}$$

It reveals the influences of the Taylor expansion on the strict unitarity of the exponential $\exp(-i\hat{h}\Delta t)$. In Fig. 5, the time evolution of the relative particle number deviation $|[N(t) - N_{init.}]/N_{init.}|$ is shown with different Δt and m values. Similar to the conservation of the total energy (see Fig. 3), the particle number is better conserved with smaller Δt and larger m values; except for the unstable evolution with $\Delta t = 0.1$ fm/c
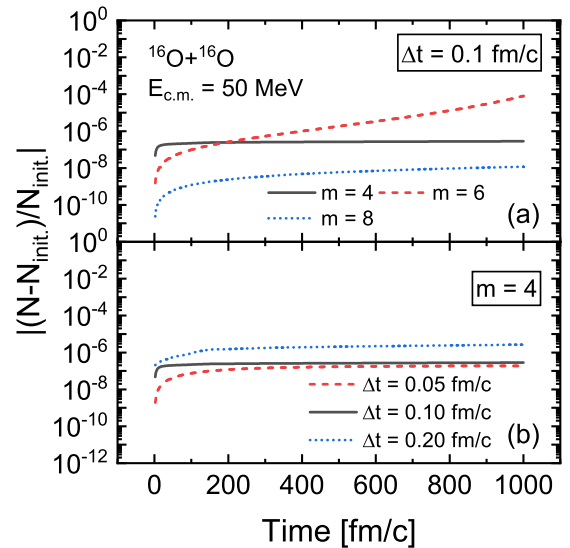

FIG. 5. Same as Fig. 3 but for the relative particle number deviation $|[N(t) - N_{init.}]/N_{init.}|$ with respect to the initial particle number $N_{init.}$.

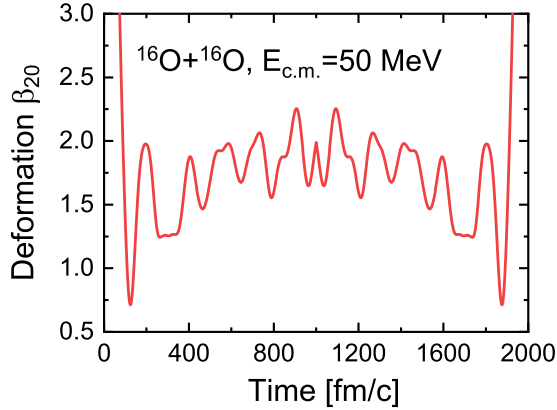FIG. 6. Time evolution of the quadrupole deformation β_{20} for the $^{16}\text{O} + {}^{16}\text{O}$ head-on collision at $E_{\text{c.m.}} = 50$ MeV. The single-particle wave functions at time $t = 1000$ fm/c are replaced by their time-reversal conjugates.

and $m = 6$. The particle number is conserved quite well for all stable evolutions, and the relative particle number deviation is around 10^{-7} at 1000 fm/c in the case of $\Delta t = 0.1$ fm/c and $m = 4$. With $\Delta t = 0.1$ fm/c, the calculations with larger $m = 10, \ 12, \ 14$ are also performed. Better conservations of particle number can be reached, and the relative deviation is as small as 10^{-14} for $m = 14$.

All in all, it is found that the momentum, total energy, and particle number are conserved with high precisions in the present TDCDFT calculations with $\Delta t = 0.1$ fm/c and $m = 4$. Therefore, they are adopted in the following investigations.

Apart from the conservation laws, another severe test of the TDCDFT is provided by the time-reversal invariance, which means that the whole system has the microscopic reversibility [30,77]. To see this property in $^{16}\text{O} + {}^{16}\text{O}$ head-on collision at $E_{\text{c.m.}} = 50$ MeV, the single-particle wave functions $\psi_k(\boldsymbol{r}, t)$ at $t = 1000$ fm/c are replaced by their time-reversal conjugates,

$$\hat{T}\psi_k(\boldsymbol{r}, t) = -i\alpha_x\alpha_z\psi_k^*(\boldsymbol{r}, t), \tag{21}$$

where α_x and α_z are Dirac matrices. With the time going on, the system should return to the state at the initial time. In Fig. 6, the time evolution of the quadrupole deformation β_{20} is shown. It is clearly seen that β_{20} evolves back precisely after replacing $\psi_k(\boldsymbol{r}, t)$ with $\hat{T}\psi_k(\boldsymbol{r}, t)$ at 1000 fm/c. Moreover, the nucleon density at $t = 2000$ fm/c is also found to agree quite well with the initial one. These results demonstrate that the time-reversal invariance is fulfilled in the present TDCDFT calculations.

V. DISSIPATION DYNAMICS

The dissipation dynamics plays an important role in heavy-ion collisions. It is responsible for the irreversible conversion of the initial collective kinetic energy into intrinsic nuclear excitations. To study the dissipation dynamics in deep-inelastic collisions, the $^{16}\text{O} + {}^{16}\text{O}$ head-on collisions with the center-of-mass energy $E_{\text{c.m.}}$ above the upper threshold of fusion are calculated. A measure of the dissipation is given by the
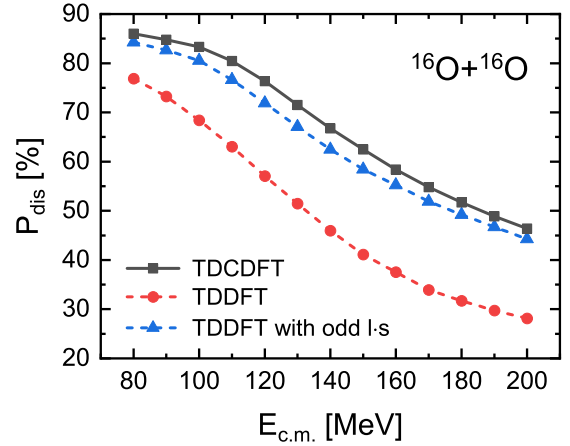

FIG. 7. Percentage of energy dissipation for the $^{16}\text{O} + {}^{16}\text{O}$ head-on collisions as a function of the center-of-mass energy $E_{\text{c.m.}}$. For comparison, the nonrelativistic TDDFT results (circle) and the ones with further inclusion of the time-odd spin-orbit terms (triangle), taken from Ref. [78], are also shown.

percentage of energy dissipation $P_{\text{dis}} = 1 - E_{\text{fin}}/E_{\text{c.m.}}$, where $E_{\text{c.m.}}$ and E_{fin} represent the initial and final collective kinetic energies, respectively.

In Fig. 7, the percentage of energy dissipation P_{dis} calculated with the TDCDFT is depicted as a function of $E_{\text{c.m.}}$ in comparison with the nonrelativistic TDDFT results, which are taken from Ref. [78]. The spin-orbit interaction has significant effects on the dissipation, since it couples the spatial motion of the nucleons with the spin degree of freedom, and gives a mechanism for the collective kinetic energy to excite the internal spin degrees of freedom [15]. It is well known that the spin-orbit interaction is from relativistic dynamics, and it is naturally taken into account in a covariant density functional. One can see from Fig. 7 that the energy dissipations P_{dis} in nonrelativistic TDDFT are much lower than the relativistic ones. The discrepancies are significantly reduced with further inclusion of the time-odd spin-orbit terms in the nonrelativistic TDDFT calculations. This reveals the fact that a covariant density functional automatically contains both time-even and time-odd spin-orbit interactions.

The features of energy dissipation could be seen more clearly through the density distributions. Figure 8 shows the density distributions of the separating ions at a given relative distance $R = 8.3$ fm for the $^{16}\text{O} + {}^{16}\text{O}$ head-on collisions with three center-of-mass energies, i.e., $E_{\text{c.m.}} = 90$, 130, and 170 MeV. With increasing $E_{\text{c.m.}}$, the density distribution becomes less diffused. This is due to the fact that the collective motion becomes faster for larger $E_{\text{c.m.}}$ and, thus, the mean field has less time to rearrange itself and more likely keeps its identity as the incident nucleus. This is also consistent with the decreased trend of the percentage of energy dissipation P_{dis} in Fig. 7, and, for the present three center-of-mass energies, the corresponding P_{dis} are respectively 84.5%, 70.9%, and 54.2% in the TDCDFT calculations. Similar features were also obtained in the nonrelativistic TDDFT calculations with the time-odd spin-orbit terms [78], while here the density distributions are more diffused in the
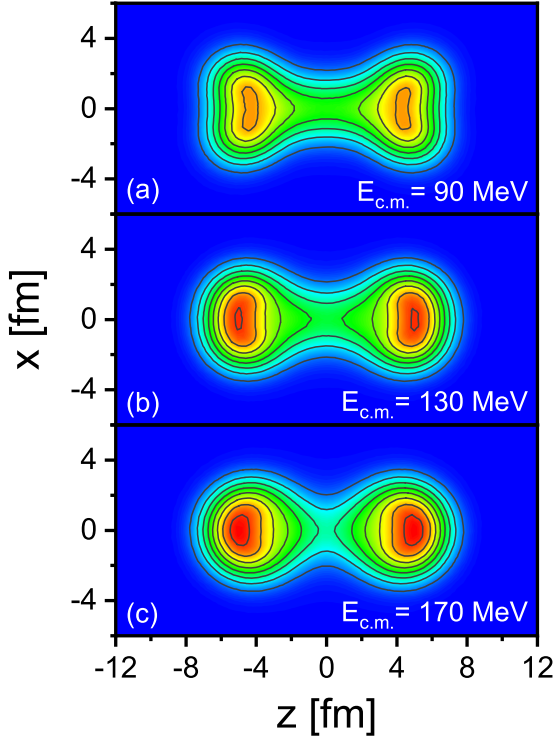
FIG. 8. Density distributions of the separating ions at a given relative distance $R = 8.3$ fm for the ^{16}O $+$ ^{16}O head-on collisions with the center-of-mass energies $E_{c.m.} = 90$ MeV (top), 130 MeV (middle), and 170 MeV (bottom). The isolines correspond to multiples of 0.02 fm^{-3}.

TDCDFT due to the slightly larger energy dissipation P_{dis} (see Fig. 7).

VI. ABOVE-BARRIER FUSION CROSS SECTION

The fusion of ^{16}O $+$ ^{16}O at above Coulomb barrier energies is one of the most important benchmarks for the early applications of TDDFT [31–36]. The primary reason is that ^{16}O is a light double-magic nucleus, and there are abundant data for the ^{16}O $+$ ^{16}O fusion cross section [79–83]. The early calculations of TDDFT gave conspicuous transparency for the collisions with low angular momenta, which was, however, not observed in experiment. This problem is known as the "fusion window anomaly," and was later resolved by the inclusion of spin-orbit interactions [84,85]. Here, the above-barrier fusion cross section of ^{16}O $+$ ^{16}O is investigated with the newly developed TDCDFT in 3D lattice space.

In the present work, the fusion cross section is calculated by

$$\sigma_{fus}(E_{c.m.}) = \frac{\pi}{2\mu E_{c.m.}} \sum_{L=0}^{\infty} (2L + 1)P_{fus}(L, E_{c.m.}), \quad (22)$$

where μ is the reduced mass of the system, and $P_{fus}(L, E_{c.m.})$ is the fusion probability for the partial wave with orbital angular momentum L at the center-of-mass energy $E_{c.m.}$. Since
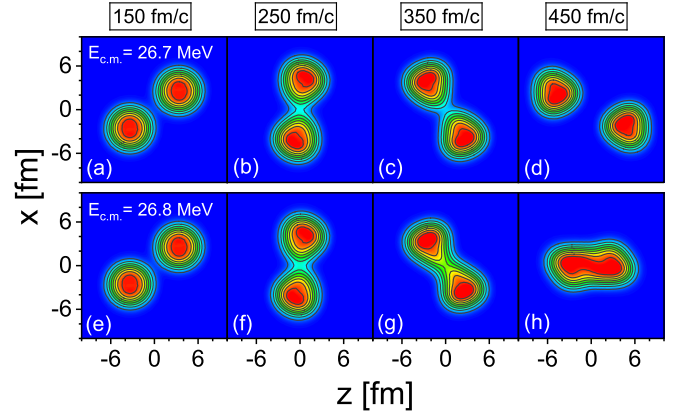

FIG. 9. Total density evolutions for the ^{16}O $+$ ^{16}O reactions with the orbital angular momentum $L = 20\hbar$. The first and second rows depict the results at the center-of-mass energies $E_{c.m.} = 26.7$ and 26.8 MeV, respectively. The isolines correspond to multiples of 0.02 fm^{-3}.

^{16}O $+$ ^{16}O is a system composed of two identical spin-zero nuclei, the cross section must be multiplied by a factor of 2 and the sum over angular momenta in Eq. (22) is restricted to even values of L. Due to the mean-field approximation in TDCDFT, the sub-barrier tunneling of the many-body wave function is not included, i.e., $P_{fus} = 0$ or 1. Such a sharp change can be smoothed by the well-known Hill-Wheeler formula [86] with a Fermi function,

$$P_{fus}(L, E_{c.m.}) = \frac{\exp(x_L)}{1 + \exp(x_L)}, \quad (23)$$

with $x_L = [E_{c.m.} - B(L)]/\varepsilon_0$. Here, the decay constant ε_0 is chosen as 0.4 MeV [87], and $B(L)$ is the position of the angular-momentum-dependent barrier.

To obtain the barriers $B(L)$ with the TDCDFT, the fusion dynamics are examined in terms of semiclassical trajectories. As an example, the total density evolutions for the ^{16}O $+$ ^{16}O reactions with $L = 20\hbar$ are shown in Fig. 9. The first and second rows depict the total density evolutions at the center-of-mass energies $E_{c.m.} = 26.7$ and 26.8 MeV, respectively. For both energies, the two incident nuclei first form a compound system with a neck [see Figs. 9(b), 9(c), 9(f), and 9(g)]. The compound system then reseparates in a short time at $E_{c.m.} = 26.7$ MeV [see Fig. 9(d)], while it fuses to a more compact system at $E_{c.m.} = 26.8$ MeV [see Fig. 9(h)]. This indicates that the barrier $B(L = 20\hbar)$ is in the range of 26.7–26.8 MeV and, thus, is taken as 26.75 MeV approximately in this work. The barriers $B(L)$ for other L values can be obtained in the same way, and for a given angular momentum L the center-of-mass energy $E_{c.m.}$ is altered with a step 0.1 MeV until the transition between not-fusion and fusion is found.

With the obtained barriers $B(L)$, the fusion probability $P_{fus}(L, E_{c.m.})$ can be further calculated via the Hill-Wheeler formula, Eq. (23). The above-barrier fusion cross sections σ_{fus} in turn obtained are shown in Fig. 10, in comparison with the data [79–83] and the nonrelativistic ones. There is an overall overestimation of the data of Fernandez et al.
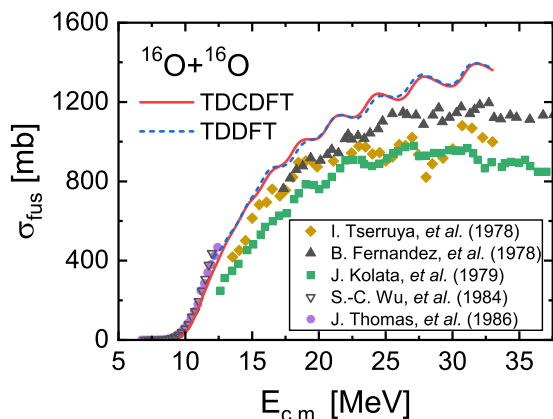
FIG. 10. Above-barrier fusion cross sections as a function of the center-of-mass energy $E_{c.m.}$ for $^{16}O + ^{16}O$ reactions. The nonrelativistic TDDFT results with the time-odd spin-orbit terms are taken from Ref. [88], and the experimental data are taken from Refs. [79–83].

[79] by around 16%. Note that the TDCDFT calculations are based on a universal functional fitted to the bulk properties of the finite nuclei, and have no free parameters coming from the reaction mechanism, so this systematic discrepancy remains small. Due to the quantization of the angular momentum L, the cross sections of the TDCDFT calculations exhibit oscillations with respect to $E_{c.m.}$. Similar oscillations can also be found in the data. Therefore, one can conclude that the newly developed TDCDFT in 3D lattice space is an effective approach to investigate the nuclear fusion processes.

For comparison, the nonrelativistic TDDFT results with the time-odd spin-orbit terms [88] are also shown in Fig. 10, and they are very close to the TDCDFT ones. Since the spin-orbit interactions are automatically included in the TDCDFT, here the problem of the fusion window anomaly is resolved naturally; otherwise the fusion cross section would be suppressed significantly [15].

VII. SUMMARY

In summary, time-dependent covariant density functional theory with the successful density functional PC-PK1 has been developed in a three-dimensional coordinate space without any symmetry restrictions, and benchmark calculations for the $^{16}O + ^{16}O$ reaction have been performed systematically. Numerical tests and two primary applications including the dissipation dynamics and the above-barrier fusion cross sections are performed. For a boosted ^{16}O, the collective kinetic energy with respect to the boost velocity agrees well with the relativistic kinetic energy, and the total momentum is conserved with a relative deviation around 10^{-5} during the time evolution. For the $^{16}O + ^{16}O$ head-on collision with the center-of-mass energy $E_{c.m.} = 50$ MeV, the total energy and particle number are conserved precisely with the relative deviations respectively of around 10^{-4} and 10^{-7} within a time evolution of 1000 fm/c, and the time-reversal invariance is fulfilled quite well. The dissipation dynamics have been investigated for the deep-inelastic head-on collisions of the $^{16}O + ^{16}O$ system. It is revealed that the obtained percentages of the energy dissipation are reasonable and similar to the nonrelativistic TDDFT results with the time-odd spin-orbit terms. The above-barrier fusion cross section of $^{16}O + ^{16}O$ is taken as another benchmark, and the experimental data are well reproduced. These systematic investigations demonstrate that the TDCDFT in a 3D lattice can be an effective approach for the future studies of nuclear dynamical processes.

[1] I. Tanihata, H. Savajols, and R. Kanungo, Prog. Part. Nucl. Phys. **68**, 215 (2013).

[2] A. B. Balantekin, J. Carlson, D. J. Dean, G. M. Fuller, R. J. Furnstahl, M. Hjorth-Jensen, R. V. F. Janssens, B.-A. Li, W. Nazarewicz, F. M. Nunes, W. E. Ormand, S. Reddy, and B. M. Sherrill, Mod. Phys. Lett. A **29**, 1430010 (2014).

[3] M. Bender, P.-H. Heenen, and P.-G. Reinhard, Rev. Mod. Phys. **75**, 121 (2003).

[4] J. Meng, ed., *Relativistic Density Functional for Nuclear Structure*, International Review of Nuclear Physics, Vol. 10 (World Scientific, Singapore, 2016).

[5] W. Kohn and L. J. Sham, Phys. Rev. **140**, A1133 (1965).

[6] P. Ring, Prog. Part. Nucl. Phys. **37**, 193 (1996).

[7] D. Vretenar, A. V. Afanasjev, G. A. Lalazissis, and P. Ring, Phys. Rep. **409**, 101 (2005).

[8] J. Meng, H. Toki, S. G. Zhou, S. Q. Zhang, W. H. Long, and L. S. Geng, Prog. Part. Nucl. Phys. **57**, 470 (2006).

[9] T. Nikšić, D. Vretenar, and P. Ring, Prog. Part. Nucl. Phys. **66**, 519 (2011).

[10] B. D. Serot and J. D. Walecka, Adv. Nucl. Phys. **16**, 1 (1986).

[11] J. D. Walecka, Ann. Phys. (NY) **83**, 491 (1974).

[12] M. M. Sharma, G. Lalazissis, J. König, and P. Ring, Phys. Rev. Lett. **74**, 3744 (1995).

[13] H. Liang, J. Meng, and S.-G. Zhou, Phys. Rep. **570**, 1 (2015).

[14] J. Meng, J. Peng, S.-Q. Zhang, and P.-W. Zhao, Front. Phys. **8**, 55 (2013).

[15] P. D. Stevenson and M. C. Barton, Prog. Part. Nucl. Phys. **104**, 142 (2019).

[16] J. Meng and P. Ring, Phys. Rev. Lett. **77**, 3963 (1996).

[17] J. Meng and P. Ring, Phys. Rev. Lett. **80**, 460 (1998).

[18] S.-G. Zhou, J. Meng, P. Ring, and E.-G. Zhao, Phys. Rev. C **82**, 011301(R) (2010).

[19] X. W. Xia, Y. Lim, P. W. Zhao, H. Z. Liang, X. Y. Qu, Y. Chen, H. Liu, L. F. Zhang, S. Q. Zhang, Y. Kim, and J. Meng, At. Data Nucl. Data Tables **121–122**, 1 (2018).

[20] J. Peng, J. Meng, P. Ring, and S. Q. Zhang, Phys. Rev. C **78**, 024313 (2008).

[21] P. W. Zhao, J. Peng, H. Z. Liang, P. Ring, and J. Meng, Phys. Rev. Lett. **107**, 122501 (2011).

[22] P. W. Zhao, N. Itagaki, and J. Meng, Phys. Rev. Lett. **115**, 022501 (2015).

[23] P. W. Zhao, Phys. Lett. B **773**, 1 (2017).

[24] T. Nikšić, D. Vretenar, and P. Ring, Phys. Rev. C **66**, 064302 (2002).

[25] N. Paar, D. Vretenar, E. Khan, and G. Colò, Rep. Prog. Phys. **70**, 691 (2007).

[26] N. Paar, Y. F. Niu, D. Vretenar, and J. Meng, Phys. Rev. Lett. **103**, 032502 (2009).

[27] Y. Niu, N. Paar, D. Vretenar, and J. Meng, Phys. Lett. B **681**, 315 (2009).

[28] E. Runge and E. K. U. Gross, Phys. Rev. Lett. **52**, 997 (1984).

[29] Y. M. Engel, D. M. Brink, K. Goeke, S. J. Krieger, and D. Vautherin, Nucl. Phys. A **249**, 215 (1975).

[30] P. Bonche, S. Koonin, and J. W. Negele, Phys. Rev. C **13**, 1226 (1976).

[31] S. Koonin, Phys. Lett. B **61**, 227 (1976).

[32] R. Y. Cusson, R. K. Smith, and J. A. Maruhn, Phys. Rev. Lett. **36**, 1166 (1976).

[33] S. E. Koonin, K. T. R. Davies, V. Maruhn-Rezwani, H. Feldmeier, S. J. Krieger, and J. W. Negele, Phys. Rev. C **15**, 1359 (1977).

[34] H. Flocard, S. E. Koonin, and M. S. Weiss, Phys. Rev. C **17**, 1682 (1978).

[35] P. Bonche, B. Grammaticos, and S. Koonin, Phys. Rev. C **17**, 1700 (1978).

[36] K. T. R. Davies, H. T. Feldmeier, H. Flocard, and M. S. Weiss, Phys. Rev. C **18**, 2631 (1978).

[37] P. A. M. Dirac, Math. Proc. Cambridge **26**, 376 (1930).

[38] J. W. Negele, Rev. Mod. Phys. **54**, 913 (1982).

[39] C. Simenel, Eur. Phys. J. A **48**, 152 (2012).

[40] T. Nakatsukasa, K. Matsuyanagi, M. Matsuo, and K. Yabana, Rev. Mod. Phys. **88**, 045004 (2016).

[41] C. Simenel and A. S. Umar, Prog. Part. Nucl. Phys. **103**, 19 (2018).

[42] C. Simenel, Phys. Rev. Lett. **105**, 192701 (2010).

[43] K. Sekizawa and K. Yabana, Phys. Rev. C **88**, 014614 (2013).

[44] K. Sekizawa and K. Yabana, Phys. Rev. C **93**, 054616 (2016).

[45] Z. Wu and L. Guo, Phys. Rev. C **100**, 014612 (2019).

[46] P. Goddard, P. Stevenson, and A. Rios, Phys. Rev. C **92**, 054610 (2015).

[47] A. Bulgac, P. Magierski, K. J. Roche, and I. Stetcu, Phys. Rev. Lett. **116**, 122504 (2016).

[48] Y. Tanimura, D. Lacroix, and S. Ayik, Phys. Rev. Lett. **118**, 152501 (2017).

[49] G. Scamps and C. Simenel, Nature **564**, 382 (2018).

[50] L. Guo and T. Nakatsukasa, EPJ Web Conf. **38**, 09003 (2012).

[51] A. Umar and V. Oberacker, Nucl. Phys. A **944**, 238 (2015).

[52] C. Yu and L. Guo, Sci. China Phys. Mech. Astron. **60**, 092011 (2017).

[53] L. Guo, C. Shen, C. Yu, and Z. Wu, Phys. Rev. C **98**, 064609 (2018).

[54] L. Guo, C. Simenel, L. Shi, and C. Yu, Phys. Lett. B **782**, 401 (2018).

[55] J. A. Maruhn, P. G. Reinhard, P. D. Stevenson, J. R. Stone, and M. R. Strayer, Phys. Rev. C **71**, 064328 (2005).

[56] P. G. Reinhard, L. Guo, and J. A. Maruhn, Eur. Phys. J. A **32**, 19 (2007).

[57] B. Schuetrumpf, W. Nazarewicz, and P.-G. Reinhard, Phys. Rev. C **93**, 054304 (2016).

[58] A. S. Umar, J. A. Maruhn, N. Itagaki, and V. E. Oberacker, Phys. Rev. Lett. **104**, 212503 (2010).

[59] K.-H. Müller, Nucl. Phys. A **372**, 459 (1981).

[60] R. Y. Cusson, P. G. Reinhard, J. J. Molitoris, H. Stöcker, M. R. Strayer, and W. Greiner, Phys. Rev. Lett. **55**, 2786 (1985).

[61] J. J. Bai, R. Y. Cusson, J. Wu, P. G. Reinhard, H. Stoecker, W. Greiner, and M. R. Strayer, Z. Phys. A **326**, 269 (1987).

[62] D. Vretenar, H. Berghammer, and P. Ring, Phys. Lett. B **319**, 29 (1993).

[63] D. Vretenar, H. Berghammer, and P. Ring, Nucl. Phys. A **581**, 679 (1995).

[64] Y. Zhang, H. Z. Liang, and J. Meng, Chin. Phys. C **33**, 113 (2009).

[65] Y. Zhang, H. Liang, and J. Meng, Int. J. Mod. Phys. E **19**, 55 (2010).

[66] K. Hagino and Y. Tanimura, Phys. Rev. C **82**, 057301 (2010).

[67] Y. Tanimura, K. Hagino, and H. Z. Liang, Prog. Theor. Exp. Phys. **2015**, 073D01 (2015).

[68] Z. X. Ren, S. Q. Zhang, and J. Meng, Phys. Rev. C **95**, 024313 (2017).

[69] Z. X. Ren, S. Q. Zhang, P. W. Zhao, N. Itagaki, J. A. Maruhn, and J. Meng, Sci. China Phys. Mech. Astron. **62**, 112062 (2019).

[70] Z. X. Ren, P. W. Zhao, S. Q. Zhang, and J. Meng, Nucl. Phys. A **996**, 121696 (2020).

[71] Z. X. Ren, P. W. Zhao, and J. Meng, Phys. Lett. B **801**, 135194 (2020).

[72] P. W. Zhao, Z. P. Li, J. M. Yao, and J. Meng, Phys. Rev. C **82**, 054319 (2010).

[73] R. van Leeuwen, Phys. Rev. Lett. **82**, 3863 (1999).

[74] W. Greiner, *Relativistic Quantum Mechanics: Wave Equations* (Springer, New York, 2013).

[75] J. A. Maruhn, P. G. Reinhard, P. D. Stevenson, and A. S. Umar, Comput. Phys. Commun. **185**, 2195 (2014).

[76] J. Eastwood and D. Brownrigg, J. Comput. Phys. **32**, 24 (1979).

[77] P. Ring and P. Schuck, *The Nuclear Many-Body Problem* (Springer, New York, 2004).

[78] G.-F. Dai, L. Guo, E.-G. Zhao, and S.-G. Zhou, Phys. Rev. C **90**, 044609 (2014).

[79] B. Fernandez, C. Gaarde, J. Larsen, S. Pontoppidan, and F. Videbaek, Nucl. Phys. A **306**, 259 (1978).

[80] I. Tserruya, Y. Eisen, D. Pelte, A. Gavron, H. Oeschler, D. Berndt, and H. L. Harney, Phys. Rev. C **18**, 1688 (1978).

[81] J. J. Kolata, R. M. Freeman, F. Haas, B. Heusch, and A. Gallmann, Phys. Rev. C **19**, 2237 (1979).

[82] S.-C. Wu and C. Barnes, Nucl. Phys. A **422**, 373 (1984).

[83] J. Thomas, Y. T. Chen, S. Hinds, D. Meredith, and M. Olson, Phys. Rev. C **33**, 1679 (1986).

[84] A. S. Umar, M. R. Strayer, and P. G. Reinhard, Phys. Rev. Lett. **56**, 2793 (1986).

[85] P.-G. Reinhard, A. S. Umar, K. T. R. Davies, M. R. Strayer, and S.-J. Lee, Phys. Rev. C **37**, 1026 (1988).

[86] D. L. Hill and J. A. Wheeler, Phys. Rev. **89**, 1102 (1953).

[87] H. Esbensen, Phys. Rev. C **85**, 064611 (2012).

[88] C. Simenel, R. Keser, A. S. Umar, and V. E. Oberacker, Phys. Rev. C **88**, 024617 (2013).